Atomic Data and Nuclear Data Tables 119 (2018) 303-313

Contents lists available at ScienceDirect

Atomic Data and Nuclear Data Tables

journal homepage: www.elsevier.com/locate/adt

Converged and consistent high-resolution low-energy electron–hydrogen scattering. I. Data below $n = 4$ threshold for applications in stellar physics

Jakub Benda *, Karel Houfek

Institute of Theoretical Physics, Faculty of Mathematics and Physics, Charles University, V Holešovičkách 2, Praha 8, 180 00, Czech Republic

ARTICLE INFO

Article history:
Received 10 February 2017
Accepted 23 February 2017
Available online 8 April 2017

Keywords:
Exterior complex scaling
Electron–hydrogen scattering

ABSTRACT

In this article we present converged datasets containing scattering data for collisions of electrons on the atomic hydrogen for total energies below the $n = 4$ excitation threshold. The data have been obtained from an *ab initio* solution of the two-electron Schrödinger equation in the B-spline basis with the exterior complex scaling boundary condition and are well converged both radially and in terms of partial waves, often to a greater accuracy than currently available data. The data consist of partial T-matrices and can be combined to various secondary quantities, most notably the differential and integral cross sections. We compare the cross sections with previously published theoretical and experimental results and with available data from on-line databases. It is demonstrated that the new data are superior to the generally available results. The consistency of the cross section datasets is checked using the theorem of detailed balance. The energy sampling is fine enough to contain all major resonances in the considered energy range.

* Corresponding author.
E-mail addresses: jakub.benda@seznam.cz (J. Benda), karel.houfek@mff.cuni.cz (K. Houfek).

http://dx.doi.org/10.1016/j.adt.2017.02.003
0092-640X/

Contents

1. Introduction

The electron–hydrogen collision data are frequently used in astrophysics, particularly in the stellar physics for calculation of spectral line profiles in various dynamical and thermal conditions [1–4], and in the physics of the interstellar gas [5] as one of the cooling mechanisms of the material, or in estimation of the particle energy deposition in the universe [6]. Apart from the astrophysics, electron–hydrogen scattering is also a vital ingredient for the simulation of processes in the industrial plasmas in thermonuclear reactors [7,8]. Most applications use the temperature-averaged cross sections – *collision rates* – which are calculated from the complete energetical dependence of the cross sections, typically with Maxwellian weighting. Due to the rapid decay of the Maxwellian distribution, for low temperatures (e.g. in cool stellar gas) the low-energy part of the cross-section datasets just above the threshold of the transition is very important and needs to be resolved down to all major resonances. In typical neutral plasmas, both in stars and in tokamaks, the collisions of atoms with electrons happen much more frequently than collisions with positive ions, because at the same thermal energy the electrons have greater velocity.

There are several possible outcomes from a collision of an electron and a neutral hydrogen atom:

$$e^- + \mathrm{H}(n, l, m) \to e^- + \mathrm{H}(n', l', m')\,,$$
$$e^- + \mathrm{H}(n, l, m) \to e^- + e^- + p^+\,,$$
$$e^- + \mathrm{H}(n, l, m) \to \mathrm{H}^- + \gamma\,,$$

which are the elastic scattering, excitation and de-excitation (including spin-flip), ionization, and radiative electron capture, respectively. These processes have been thoroughly studied in the past with various theoretical approaches and large amount of data is already available, possibly with the exception of the radiative capture, which requires the calculations to include the coupling to the electro-magnetic field. For the same reason radiation is also disregarded in the other two processes.

Some collections of electron–hydrogen scattering data were published in the past and we have included most of them in the graphs at the end of the article. Before the voluminous experimental and theoretical review by Bederson and Kieffer [9] only rudimentary data had been calculated, often using a hand-crafted close-coupling expansion and rarely converged to better accuracy then a few tens per cent.

The first noteworthy collection of accurate elastic and non-elastic data is due to Callaway [10], who used the straight-forward close-coupling calculation with a handful of states to calculate the cross sections for the transitions 1s–1s, 1s–2s and 1s–2p. Only total angular momenta $L \leq 3$ were included in the calculation.

The collision strengths to 2s and 2p states between the $n' = 2$ threshold and the ionization threshold were recomputed by Scholtz et al. [11]. They used the intermediate-energy R-matrix (IERM) method for low partial waves to account for the continuum coupling, the standard R-matrix for intermediate partial waves, and the second-order plane wave Born approximation for higher partial waves. The data curves are very smooth, as they lack most resonances. The data compare well with [10].

The extensive calculation of Callaway [12] has a similar scope as the present article and for the first time presented the cross sections for scattering on excited states.

Aggarwal et al. [13] published collision strength datasets for all transitions $n \to n'$, where $n \leq n'$, $n = 1, 2, 3, 4$, at energies from the transition threshold to a few eV above the ionization threshold. Their data are very finely sampled and contain a large amount of physical resonances, which have correct positions. However, as demonstrated in the graphs below, the absolute values of the cross sections are offset by an unexplained shift from the correct values.

The review by Callaway [14] summarizes results obtained up to 1994. Among others it points out some inaccuracies in [13] stemming from the omission of the continuum channels from the R-matrix basis.

Another recalculation of the three lowest transitions 1s–1s, 1s–2s and 1s–2p between the $n = 2$ and $n = 3$ thresholds has been done by Bartschat [15] using the R-matrix with pseudo-states (RMPS) method. These data were compared to the results of the

converged close coupling method (CCC, [16]) and belong currently among the reference data for electron–hydrogen scattering.

Anderson et al. [17] used the RMPS method to calculate the cross sections for transitions $n, l \to n', l'$, where $n < n'$, with the aim to produce relevant data for fusion plasma simulations. They used 15 physical states, 24 pseudo-states and $R_A = 140\,a_0$ as the radius of the inner region. However, this radius is not appropriate for transitions between excited states.

Bartlett [18] calculated the cross sections for transitions from the ground state to $n = 3$ states at a small range of energies to demonstrate the accuracy of the exterior complex scaling (ECS) method.

To sum up, some of the existing publications focus on providing rich variety of datasets, some focus on accuracy of the results for a few particular transitions, some illustrate an efficient solution method, but none of them does really combine all these viewpoints together, with explicit consideration of consistency of the datasets and their good convergence.

There are also a few on-line databases that contain the scattering data of interest. The most comprehensive is the dataset in the Aladdin database [19] calculated by Bray and Stelbovics [20] using the CCC method. Their data for elastic transitions are in perfect agreement with [15], but the same calculation setup has been used for higher transitions (up to $n = 4$), which raises doubts, whether they are sufficiently converged with respect to the basis size. Analogical CCC data are contained in LXcat database [21]. Another database is that of NIST [22], which contains only optically allowed transitions from the ground state (up to $n = 10$), produced by BE-scaling of the plane wave Born approximation results [23,24]. These data are not meant for the low-energy usage and there are very few points below the ionization threshold, if any. There is also another database by NIST [25] containing ground state elastic data produced by Salvat et al. [26], based on the Dirac equation with a model potential.

The scattering of electrons on hydrogen atoms, though well understood, still has a few pitfalls. The low-energy scattering on atomic hydrogen is dominated by its huge polarizability, which requires accurate inclusion of a large surrounding space in the numerical solution [27]. This problem is often circumvented by consideration of a truncated Coulombic interaction only, e.g. in the Debye plasmas [28,29], but for environments with low density (e.g. stellar atmospheres) it provides wrong results [30]. One of the reasons for the necessity of inclusion of the large surrounding space is the long-range dipole coupling between the channels. It is so strong that for optically allowed transition between energetically degenerated levels it gives rise to infinite cross section [31,32]. Another approach is to radially extrapolate the cross section as in [18], but this produces acceptable results only for excitations from the ground state (or de-excitations into the ground state); for scattering on excited targets it is not sufficient. For energies below or slightly above the ionization threshold this problem is solved by the R-matrix method, where the outer region considers only a few channels and can be made very large, and also by the channel reduction presented in [33], which employs an equivalent idea and is applicable to all direct grid-based methods, including the below mentioned exterior complex scaling.

In this paper we focus only on elastic scattering and inelastic transitions between all states – including magnetic sub-levels – for total atomic and projectile energies in the range from $E_{\mathrm{tot}} = -1$ Ry to $E_{\mathrm{tot}} = -0.0625$ Ry. This includes the states with the principal quantum number $n \leq 3$. A particular attention has been given to accurate simulation of the collisions right above the excitation thresholds, where the long-range multipole effects are more pronounced than elsewhere and where the existing data are mostly deficient, even though particularly those energies are of extreme importance for calculation of collisional rates at low temperatures. The chosen energies do not allow for ionization of the hydrogen target, which is why we do not discuss here the ionization data or high-energy datasets generally.

We intend to publish more data in follow-up articles, for energies up to a region where the widely used perturbation methods like the Born approximation are valid (∼1 keV). The data will be provided through a web-based database interface introduced in [34] and via the VAMDC portal [35].

2. Method

The typical method of choice when producing the scattering datasets is the R-matrix method [36], which is easily applicable to many impact energies and transitions in one run. However, to achieve this the method starts with a diagonalization of a huge many-electron Hamiltonian matrix, size of which strongly depends on the number of electrons, on the largest considered angular momentum of the electrons and on the number of states in the basis. The diagonalization then becomes costly in terms of the required computer memory and storage capacity. For this reason the R-matrix calculations mostly deal with low-lying states, in particular with the scattering on the ground state, where the Hamiltonian matrix can be kept small.

We chose a different method, which is the direct solution of the Schrödinger equation in the B-spline basis with the exterior complex scaling (ECS) boundary condition, where the matrix is not diagonalized, but iteratively solved for each initial atomic state and projectile impact energy [37]. This can be quite effective, because the matrix is very sparse and the iterative solution method uses just multiplication by the matrix. Also, every separate calculation can be run on a different computer concurrently, which simplifies the parallelization. Moreover, every calculation can have different radial and angular basis, as needed for the specific impact energy and atomic states of interest. We used the free implementation published in [34,38] with all recent updates [33,39].

Unlike a typical presentation of scattering data, where the whole dataset is calculated with fixed parameters, we took advantage from the ECS approach and ran several calculations for every data point to ensure convergence of the resulting cross sections in all parameters, namely: the radial grid size and spacing, the included angular momenta of the individual electrons and the number of total angular momenta considered. The convergence in each of these parameters has been pursued to 0.5% and so the overall accuracy of the present data should be well below 5%, which was our target. The typical inner-region radii as defined in [33] were $R_a = 100$–300 a.u., the (outer) grid size often up to $R_0 \sim 10^5$ a.u., the number of coupled angular momentum states $N_L = n_L\tilde{L}$, where $n_L = 4$–7 and $\tilde{L}$ is equal to the total angular momentum L for low partial waves and somewhat smaller for high partial waves. Systems with total angular momentum greater than $L = 20$ were calculated in a non-exchange approximation. This reduces the angular basis approximately to half and also allows calculation of the singlet or triplet configuration only, as their contributions are then equal.

3. Results

The results of the calculations have the form of the scattering partial T-matrices $T^{LS}_{fi,\ell}(k_i)$ for each initial state i, final state f, partial wave ℓ, total angular momentum L, total spin S and impact energy $E_i = \frac{1}{2}k_i^2$ (in atomic units). They are defined as

$$\sum_{\ell L} T^{LS}_{fi,\ell}(k_i) Y_\ell^{m_i - m_f}(\hat{\mathbf{k}}_f) = \langle \Psi_f^S | H_{\mathrm{int}} | \Psi_i^{S(+)} \rangle \,,$$

with the notation introduced in [38]. These T-matrices can be combined to provide the integral cross sections

$$\sigma_{fi}(k_i) = \sum_{S\in\{0,1\}} \sum_{\ell} \frac{2S+1}{4} \frac{k_f^2}{k_i^2} \left| \sum_{L} T^{LS}_{fi,\ell}(k_i) \right|^2 ,$$

but also many other quantities like the differential cross sections for arbitrary-direction impact, spin asymmetry, momentum transfer, spin-flip etc. All quantities are accessible from the above-mentioned web interface with arbitrary sampling possible via the Akima spline interpolation of the calculated data points [40]. This paper presents only the cross sections averaged over initial magnetic sublevels and summed over final magnetic sublevels, because only such data can be compared to existing data.

In the figures we show the collision strengths for individual transitions

$$\Omega_{fi}(k_i) = (2l_i + 1)k_i^2 \sigma_{fi}(k_i)$$

compared with earlier published results from other calculations or measurements. Assignment of the figures to the transitions is shown in Table A. Some figures demonstrate the consistency of the datasets in terms of the detailed balance theorem, which states that

$$\Omega_{fi}(k_i) = \Omega_{if}(k_f).$$

The new results generally match the older ones, where available, within 10%. The comparison has been done most notably with the calculations of Callaway [12] and of Aggarwal et al. [13], and with the cross sections contained in the Aladdin database.

The variational close-coupling results of Callaway are very close to the present ones. Some discrepancies stem from the fact that Callaway included just a few partial waves. This is apparent e.g. in the inset within the Graph 1; in fact, the data points would coincide with the present data if only partial waves $\ell \leq 3$ were considered. For the higher transitions the original cross sections tend to be larger than more recent data.

The comprehensive calculation by Aggarwal matches very well the resonance structure, but the absolute values are slightly offset with respect to the calculation of Bartlett [18] and the new results. The largest difference within the inspected energy range is for the cross sections from the 1s state to higher states; it reaches 12%. Elsewhere the agreement is better.

Only the Aladdin database contains data for all transitions calculated in this work. Compared to the R-matrix calculations these data are much coarser. This is a feature of the employed CCC method, which – similarly to the ECS method – can be applied only to a single energy at a time. According to the brief information mentioned in the Aladdin database all the points have been calculated using the same calculation setup. While the agreement between the CCC and present results is very satisfactory for transitions between the low states, the agreement for transitions from or to the $n = 3$ level is worse and the elastic data are very different. The discrepancies are stronger in the vicinity of the thresholds, which is the region with strong influence of the long-range induced dipole interaction. The method used in the present calculation has been specifically constructed to deal with this interaction [33], so we suppose that the Aladdin data have been insufficiently converged with respect to the radius. The CCC disguises the radial range in the range of the chosen Laguerre basis states. The CCC results that are different from the preset data thus may suffer from an insufficient basis. The largest discrepancy occurs in the case of the elastic transitions on excited states, namely in Graphs 5, 8, 9c, 11c, 13c. It is known that calculations of these data points require a huge amount of slowly converging partial wave contributions. We did our calculations up to $L \sim 30$–40, where the sum seems to converge within 1%. We suppose that the observed discrepancy arises in a premature $T_\ell \sim 1/\ell^3$ extrapolation of high partial waves calculated by the CCC method, possibly in conjunction with a modest Laguerre basis. Incidentally, all Aladdin elastic collision strengths go to zero at the opening of the appropriate threshold. This is correct behavior for the ground state elastic scattering, where the $E_i \to 0+$ limit of the cross section is a constant proportional to the squared scattering length.[1] But for elastic scattering on excited states the induced dipole interaction makes the cross section diverge with the impact energy as $1/E_i$, so the elastic collision strength tends to a constant [32].

Table A
Index of figures that contain collision data for individual transitions. The first of the two numbers for every transition is the number of the graph containing the collision strengths summed over all final magnetic sub-levels and averaged over all initial magnetic sublevels. The second number is the number of the graph with a verification of the detailed balance theorem for the transition. The degenerate optically allowed transitions (e.g. 2s–2p) are omitted, because in the non-relativistic approximation used in this work the long-range dipole coupling of these levels gives rise to infinite cross sections [31].

		Final state					
		1s	2s	2p	3s	3p	3d
Initial state	1s	1	2,10	2,10	3,12	3,12	3,12
	2s	4,10	5		6,14	6,14	6,14
	2p	4,10		8	7,14	7,14	7,14
	3s	9,12	9,14	9,14	9		9,15
	3p	11,12	11,14	11,14		11	
	3d	13,12	13,14	13,14	13,15		13

The calculation by Anderson et al. [17] has a large scope in terms of transitions and energies covered. However, the paper contains only the derived thermally averaged collision rates. The cross section is illustrated only for two selected transitions, of which only one (2s–3p) matters for this work. Compared to the present data, some resonances seem to be slightly shifted. Also, several authors disputed the overall accuracy of the collision rate datasets for various higher transitions, e.g. [42,43].

4. Conclusion

This paper contributes consistent and both radially and angularly converged theoretical data for collisions of electrons with neutral hydrogen atoms for energies below the $n = 4$ threshold. The data are finely sampled and contain all major resonances. We have compared the results with available data and found reasonable agreement. The error of the calculated results is expected to be smaller than 1% for most studied energies. In the vicinity of thresholds and around narrow resonances the error may be larger, but below 5%.

Acknowledgments

The study was supported by the Charles University in Prague, project GA UK No. 730214, and by the project SVV-260320.

Computational resources were provided by the CESNET LM2015042 and the CERIT Scientific Cloud LM2015085, provided under the program "Projects of Large Research, Development, and Innovations Infrastructures".

This work was supported by The Ministry of Education, Youth and Sports from the Large Infrastructures for Research, Experimental Development and Innovations project "IT4Innovations National Supercomputing Center LM2015070".

[1] The scattering lengths calculated when composing the present datasets were $a_s = 5.99\,a_0$ for singlet and $a_s = 1.78\,a_0$ for triplet configuration. This compares within 1% with [41].

References

[1] M. Karlický, et al., Collisional excitation and ionization of hydrogen by return current in solar flares, Astron. Astrophys. 416 (2004) L13–L16.
[2] B. Kučerová, et al., Time-dependent spectral-feature variations of stars displaying the B[e] phenomenon, Astron. Astrophys. 554 (2013) A143.
[3] J. Štěpán, P. Heinzel, Scattering polarization in solar flares, Astrophys. J. 778 (2013) L6.
[4] R.M. Sainz, et al., Depolarizing collisions with hydrogen: Neutral and singly ionized alkaline earths, Astrophys. J. 788 (2014) 118.
[5] S.R. Furlanetto, M.R. Furlanetto, Spin-exchange rates in electron-hydrogen collisions, Mon. Not. R. Astron. Soc. 374 (2007) 547–555.
[6] T. Kanzaki, M. Kawasaki, Electron and photon energy deposition in the Universe, Phys. Rev. D 78 (2008) 103004.
[7] G.M. McCracken, et al., Evidence for volume recombination in JET detached divertor plasmas, Nucl. Fusion 38 (1998) 619.
[8] V.S. Lisitsa, et al., Hydrogen spectral line shape formation in the SOL of fusion reactor plasmas, Atoms 2 (2014) 195–206.
[9] B. Bederson, L.J. Kieffer, Total electron-atom collision cross sections at low energies—A critical review, Rev. Modern Phys. 43 (1971) 601–640.
[10] J. Callaway, Scattering of electrons by hydrogen atoms, Phys. Rev. A 26 (1982) 119.
[11] T.T. Scholtz, et al., Effective collision strengths for 1s–2s and 1s–2p electron-hydrogen atom scattering, Mon. Not. R. Astr. Soc. 242 (1990) 692–697.
[12] J. Callaway, Electron-impact excitation of hydrogen atoms: Energies between the $n = 3$ and $n = 4$ thresholds, Phys. Rev. A 37 (1988) 3692–3696.
[13] K.M. Aggarwal, et al., Electron collision cross sections at low energies for all transitions between the n = 1, 2, 3, 4 and 5 levels of atomic hydrogen, J. Phys. B: At. Mol. Opt. Phys. 24 (1991) 1384–1410.
[14] J. Callaway, Effective collision strengths for hydrogen and hydrogen-like ions, At. Data Nucl. Data Tables 57 (1994) 9–20.
[15] K. Bartschat, et al., Benchmark calculations for e–H scattering between the n = 2 and n = 3 thresholds, J. Phys. B: At. Mol. Opt. Phys. 29 (1996) 5493–5503.
[16] I. Bray, A.T. Stelbovics, Convergent close-coupling calculations of electron-hydrogen scattering, Phys. Rev. A 46 (1992) 6995–7011.
[17] H. Anderson, et al., An R-matrix with pseudostates approach to the electron-impact excitation of H I for diagnostic applications in fusion plasmas, J. Phys. B: At. Mol. Opt. Phys. 33 (2000) 1255.
[18] P.L. Bartlett, et al., Differential and integrated cross sections for excitation to the 3s, 3p, and 3d states of atomic hydrogen by electron impact below the n = 4 threshold, Phys. Rev. A 74 (2006) 022714.
[19] IAEA Amdis: Aladdin database, URL http://www-amdis.iaea.org/infoaladdin.php. (Accessed 3 January 2017).
[20] I. Bray, A.T. Stelbovics, Calculation of electron scattering on hydrogenic targets, Adv. At. Mol. Opt. Phys. 35 (1995) 209.
[21] LXcat, CCC database, URL https://nl.lxcat.net/home/. (Accessed 3 January 2017).
[22] NIST Electron-impact cross sections for ionization and excitation database. URL https://www.nist.gov/pml/electron-impact-cross-sections-ionization-and-excitation-database. (Accessed 3 January 2017).
[23] Y.-K. Kim, Scaling of plane-wave Born cross sections for electron-impact excitation of neutral atoms, Phys. Rev. A 64 (2001) 032713.
[24] P.M. Stone, Y.-K. Kim, J.P. Desclaux, Electron-impact cross sections for dipole- and spin-allowed excitations of hydrogen, helium, and lithium, J. Res. Natl. Inst. Stand. Technol. 107 (2002) 327.
[25] NIST Electron Elastic-scattering Cross-section Database, SRD 64. URL https://srdata.nist.gov/SRD64/Elastic. (Accessed 3 January 2017).
[26] F. Salvat, A. Jablonski, C.J. Powell, ELSEPA—Dirac partial-wave calculation of elastic scattering of electrons and positrons by atoms, positive ions and molecules, Comput. Phys. Comm. 165 (2005) 157–190.
[27] T. O'Malley, L. Rosenberg, L. Spruch, Low-energy scattering of a charged particle by a neutral polarizable system, Phys. Rev. 125 (1961) 1300–1310.
[28] S. Kar, Y.K. Ho, Resonances in electron-hydrogen scattering in Debye plasmas, J. Phys. B: At. Mol. Opt. Phys. 44 (2011) 015001.
[29] J. Li, et al., Low energy electron-impact ionization of hydrogen atom for coplanar equal-energy-sharing kinematics in Debye plasmas, Phys. Plasmas 23 (2016) 123511.
[30] J. Rosato, H. Capes, S. Roland, Ideal coulomb plasma approximation in line shape models: Problematic issues, Atoms 2 (2014) 253–258.
[31] M.J. Seaton, Strong coupling in optically allowed atomic transitions produced by electron impact, Proc. Phys. Soc. 77 (1961) 199.
[32] M. Gailitis, R. Damburg, The influence of close coupling on the threshold behaviour of cross sections of electron-hydrogen scattering, J. Exp. Theor. Phys. 44 (1963) 1644–1649.
[33] J. Benda, K. Houfek, Reducing the dimensionality of grid based methods for electron-atom scattering calculations below ionization threshold, Comput. Phys. Comm. 213 (2017) 46–51.
[34] J. Benda, K. Houfek, Collisions of electrons with hydrogen atoms I. Package outline and high energy code, Comput. Phys. Comm. 185 (2014) 2893–2902. URL http://utf.mff.cuni.cz/data/hex.
[35] M.L. Dubernet, et al., The virtual atomic and molecular data centre (VAMDC) consortium, J. Phys. B: At. Mol. Opt. Phys. 49 (2016) 074003.
[36] P. Descouvemont, D. Baye, The R-matrix theory, Rep. Progr. Phys. 73 (2010) 036301.
[37] C.W. McCurdy, F. Martín, Implementation of exterior complex scaling in B-splines to solve atomic and molecular collision problems, J. Phys. B: At. Mol. Opt. Phys. 37 (2004) 917–936.
[38] J. Benda, K. Houfek, Collisions of electrons with hydrogen atoms II. Low-energy program using the method of the exterior complex scaling, Comput. Phys. Comm. 185 (2014) 2903–2912.
[39] J. Benda, K. Houfek, New version of hex-ecs, the B-spline implementation of exterior complex scaling method for solution of electron-hydrogen scattering, Comput. Phys. Comm. 204 (2016) 216–217.
[40] H. Akima, A new method of interpolation and smooth curve fitting based on local procedures, J. ACM 17 (1970) 589–602.
[41] A.K. Bhatia, Hybrid theory of electron-hydrogen scattering, Phys. Rev. A 75 (2007) 032713.
[42] B.P. Lavrov, A.V. Pipa, Account of the fine structure of hydrogen atom levels in the effective emission cross sections of balmer lines excited by electron impact in gases and plasma, Opt. Spectrosc. 92 (2002) 647–657.
[43] D. Wünderlich, S. Dietrich, U. Fantz, Application of a collisional radiative model to atomic hydrogen for diagnostic purposes, J. Quant. Spectrosc. Radiat. Transfer 110 (2009) 62–71.
[44] J.F. Williams, Resonance structure in inelastic scattering of electrons from atomic hydrogen, J. Phys. B: At. Mol. Opt. Phys. 21 (1988) 2107.

Explanation of Graphs

The collision strengths for individual transitions and impact energies are presented in the data graphs below. Our dataset is labeled by "Hex (2016)".

Graph 1. **The collision strengths for the elastic scattering on the ground state 1s.**
This has been calculated so many times that the nearly perfect match of the results is expected. Still, the calculation of Callaway [10] is slightly lower due to omission of the higher partial waves than $\ell = 3$; see the inset. The results of Aggarwal [13] were needed to be multiplied by 1.07 to fit into the inset. The (manually digitized) calculation by Bartschat [15] is distinguishable from the present calculation only in the inset.

Graph 2. **The collision strengths for the excitation of the ground state 1s to 2p (upper curve) and 2s (lower curve) levels.**
The data points marked by grey dots come from the measurement by Williams [44], the rest are calculations.

Graph 3. **The collision strengths for the excitation of the ground state 1s to 3s (top panel), 3p (middle) and 3d (bottom) levels.**
This graph shows perfect agreement with the other exterior complex scaling based calculation [18].

Graph 4. **The collision strengths for the de-excitation from the state 2p (upper, solid curve) and 2s (lower, broken curve) to the ground state 1s.**
This graph demonstrates perfect agreement with the data from [20].

Graph 5. **The collision strengths for the elastic scattering on the excited state 2s.**
The cross sections for the degenerate 2s–2p scattering is not shown, because in the non-relativistic approximation they are infinite.

Graph 6. **The collision strengths for excitation of the state 2s to 3s (top panel), 3p (middle) and 3d (bottom) levels.**

Graph 7. **The collision strengths for excitation of the state 2p to 3s (top panel), 3p (middle) and 3d (bottom) levels.**

Graph 8. **The collision strengths for the elastic scattering on the excited state 2p.**
The cross sections for the degenerate 2p–2s scattering is not shown, because in the non-relativistic approximation they are infinite.

Graph 9. **The collision strengths for the de-excitation from the state 3s to 1s (top panel), 2s and 2p (middle panel) states and the elastic scattering on the 3s state (bottom panel).**
The cross sections for the degenerate 3s–3p scattering is not shown, because in the non-relativistic approximation it is infinite. The collision strength for the transition 3s–3d (solid curve) has been multiplied by 2 to better fit into the image.

Graph 10. **Detailed balance for 1s–2s and 1s–2p transitions.**
The detailed balance error is calculated as $D_{ij} = 2|\Omega_{ij} - \Omega_{ji}|/|\Omega_{ij} + \Omega_{ji}|$. Except from some narrow resonance details below the $n = 3$ threshold the error D_{ij} is always better than 1%.

Graph 11. **The collision strengths for the de-excitation from the state 3p to 1s (top panel), 2s and 2p (middle panel) states and the elastic scattering on 3p state (bottom panel).**
The cross sections for the degenerate 3p–3s and 3p–3d scattering is not shown, because in the non-relativistic approximation they are infinite. The collision strength for the transition 3p–2s (broken curve) has been multiplied by 2 to better fit into the image. The reference data from Aladdin (empty triangles) has been adjusted by the same factor.

Graph 12. **Detailed balance for 1s–3s, 1s–3p and 1s–3d transitions.**
The detailed balance error is calculated as $D_{ij} = 2|\Omega_{ij} - \Omega_{ji}|/|\Omega_{ij} + \Omega_{ji}|$. The error D_{ij} is always better than 1%, except for missing narrow structure in $3d - 1s$ cross section just below the $n = 4$ threshold.

Graph 13. **The collision strengths for the de-excitation from the state 3d to 1s (top panel), 2s and 2p (middle panel) states and the elastic scattering on the 3d state (bottom panel).**
The cross sections for the degenerate 3d–3p scattering is not shown, because in the non-relativistic approximation it is infinite. The collision strength for the transition 3d–2s (broken curve) has been multiplied by 4 to better fit into the image. The reference data from Aladdin (empty triangles) has been adjusted by the same factor. Analogically for 3d–3s in the bottom panel.

Graph 14. **Detailed balance for 2ℓ–$3\ell'$ and $3\ell'$–2ℓ transitions.**
The detailed balance error is calculated as $D_{ij} = 2|\Omega_{ij} - \Omega_{ji}|/|\Omega_{ij} + \Omega_{ji}|$. The error D_{ij} is always better than 1%, except for a small region just below the $n = 4$ threshold.

Graph 15. **Detailed balance for the energetically degenerate transition 3s–3d.**
The detailed balance error is calculated as $D_{ij} = 2|\Omega_{ij} - \Omega_{ji}|/|\Omega_{ij} + \Omega_{ji}|$. The error D_{ij} is always better than 1%.

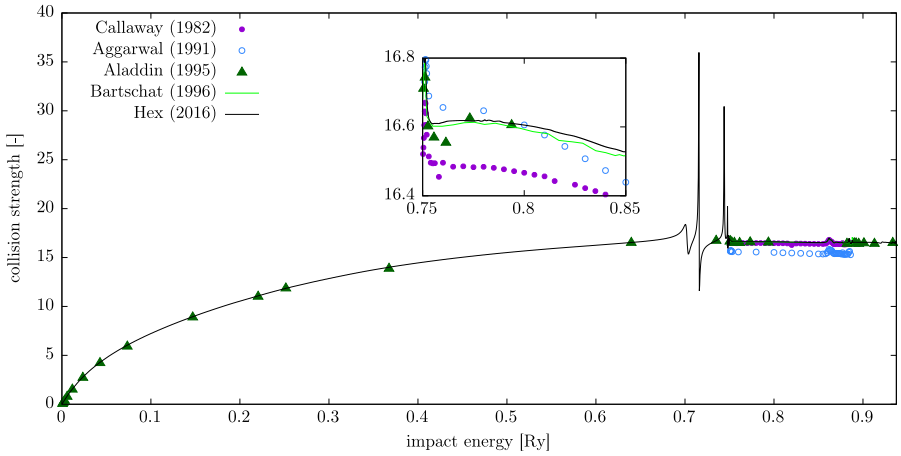

Graph 1. The collision strengths for the elastic scattering on the ground state 1s.

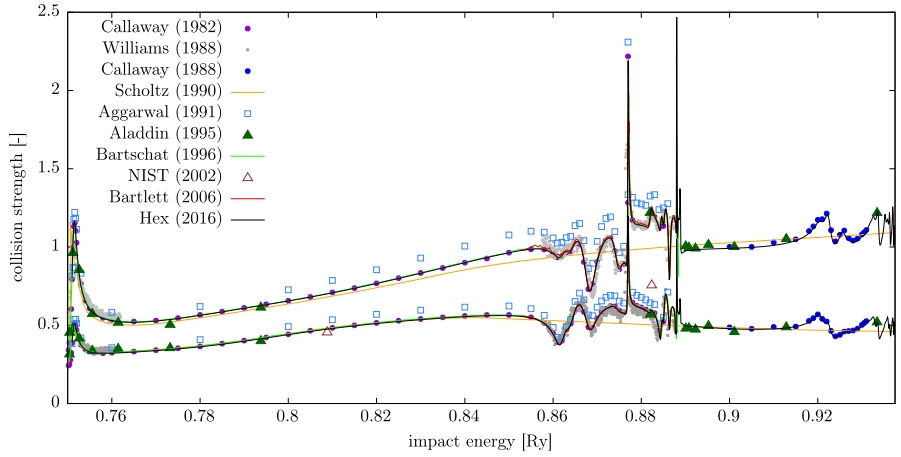

Graph 2. The collision strengths for the excitation of the ground state 1s to 2p (upper curve) and 2s (lower curve) levels.

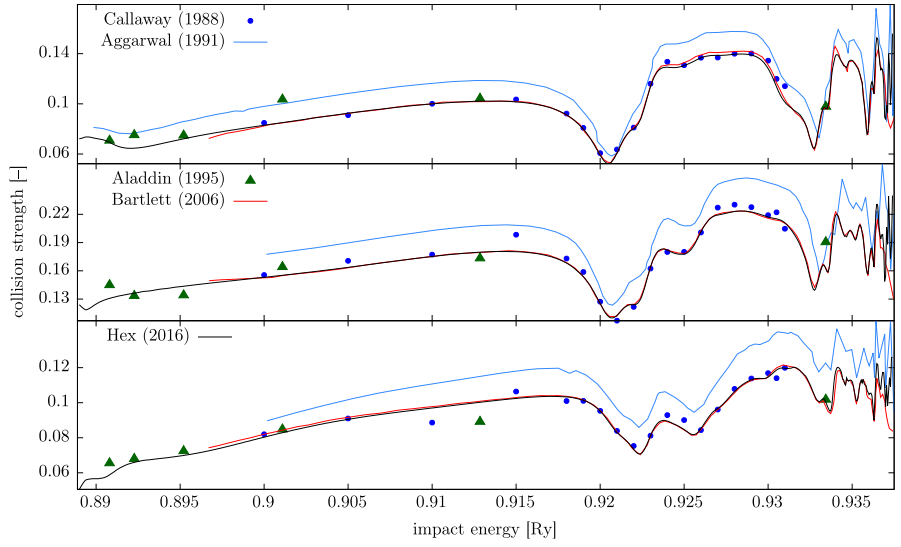

Graph 3. The collision strengths for the excitation of the ground state 1s to 3s (top panel), 3p (middle) and 3d (bottom) levels.

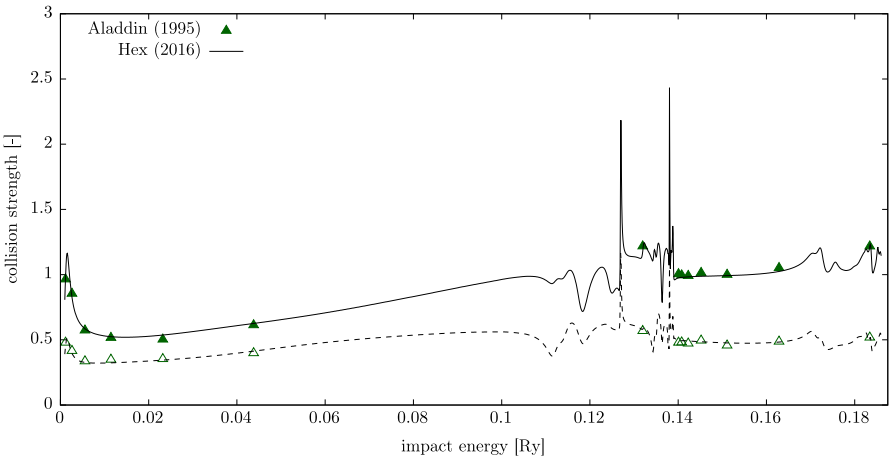

Graph 4. The collision strengths for the de-excitation from the state 2p (upper, solid curve) and 2s (lower, broken curve) to the ground state 1s.

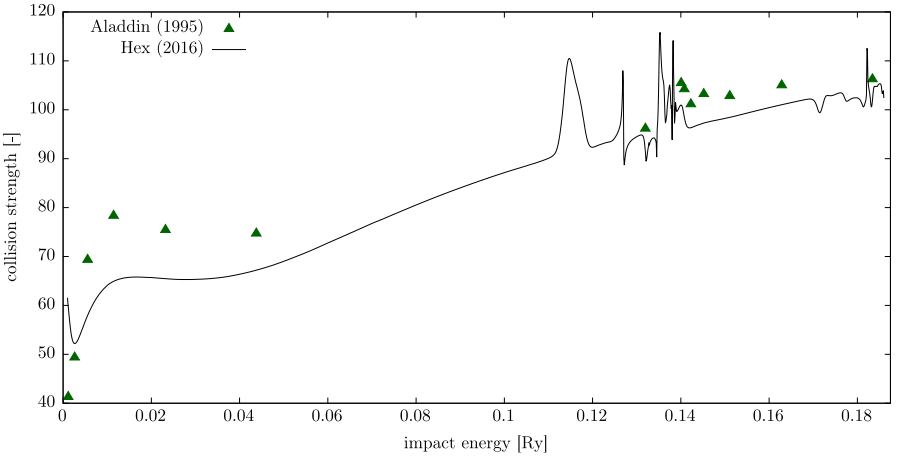

Graph 5. The collision strengths for the elastic scattering on the excited state 2s.

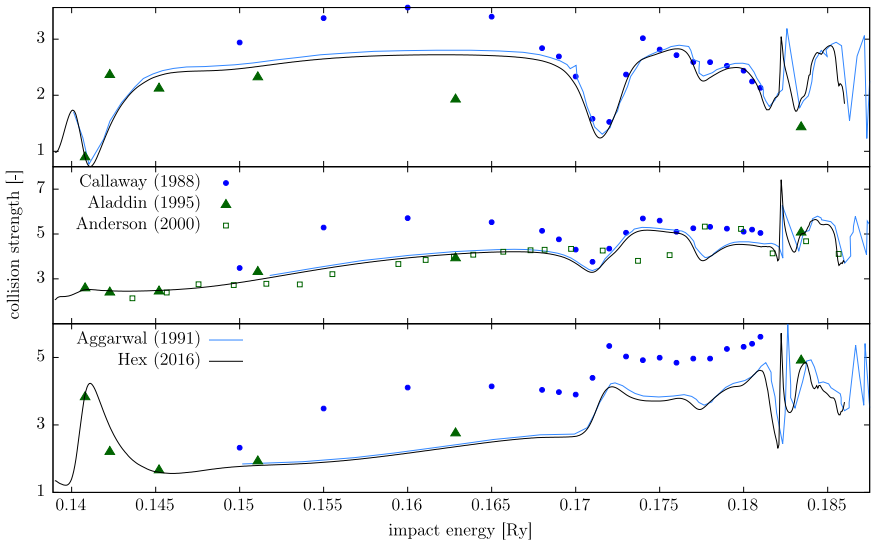

Graph 6. The collision strengths for excitation of the state 2s–3s (top panel), 3p (middle) and 3d (bottom) levels.

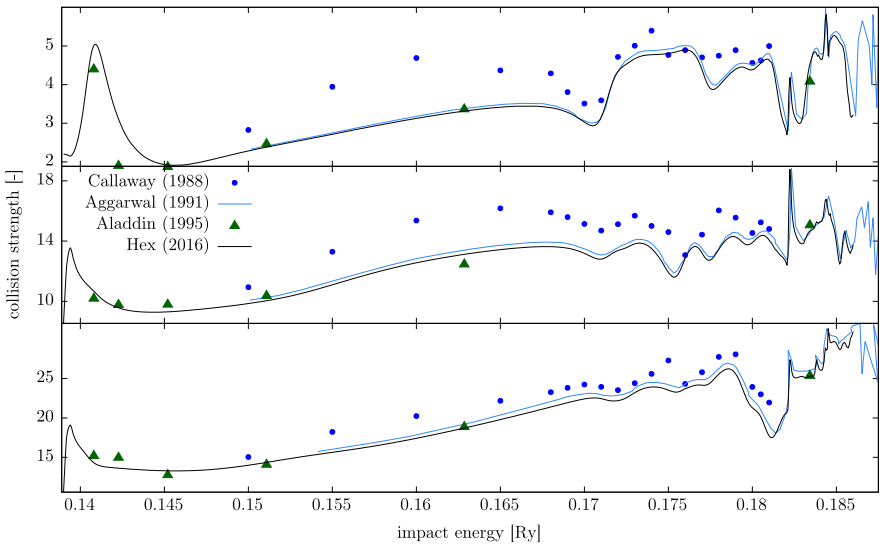

Graph 7. The collision strengths for excitation of the state 2p–3s (top panel), 3p (middle) and 3d (bottom) levels.

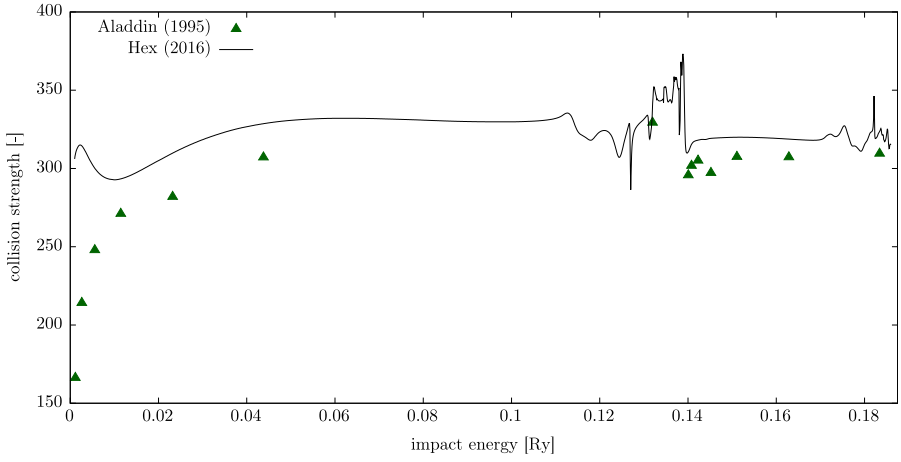

Graph 8. The collision strengths for the elastic scattering on the excited state 2p.

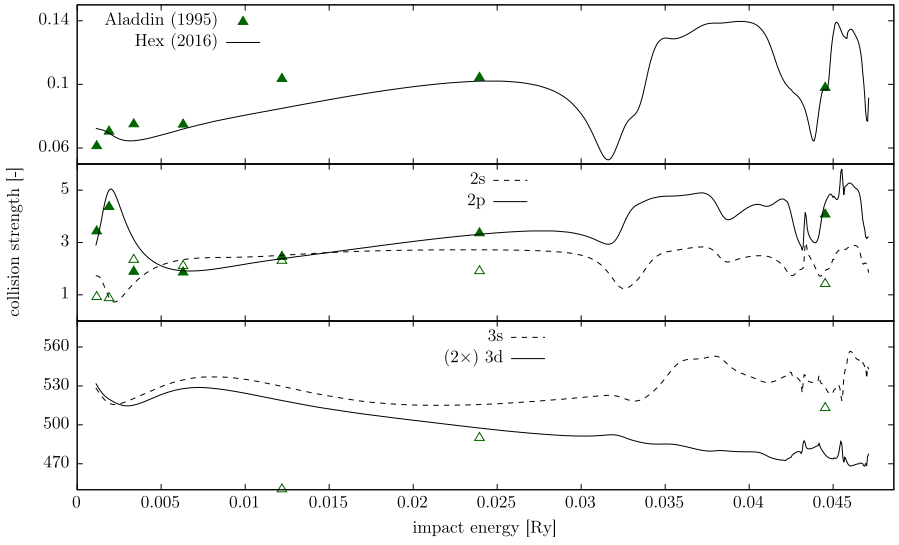

Graph 9. The collision strengths for the de-excitation from the state 3s to 1s (top panel), 2s and 2p (middle panel) states and the elastic scattering on the 3s state (bottom panel).

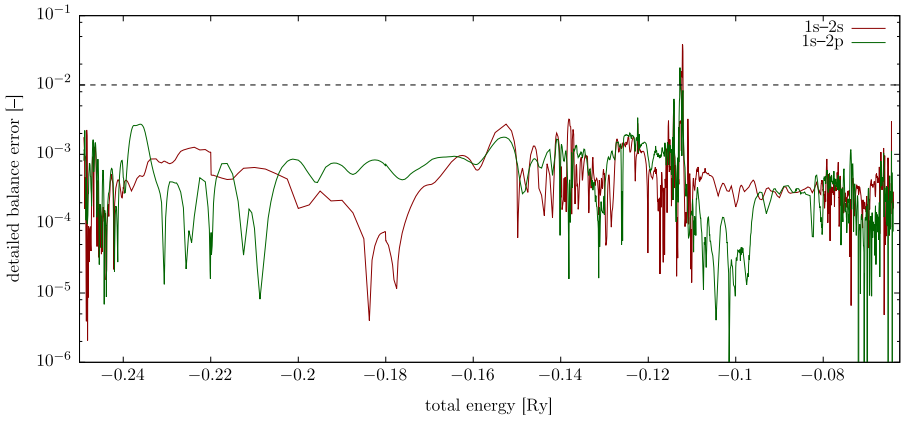

Graph 10. Detailed balance for 1s–2s and 1s–2p transitions.

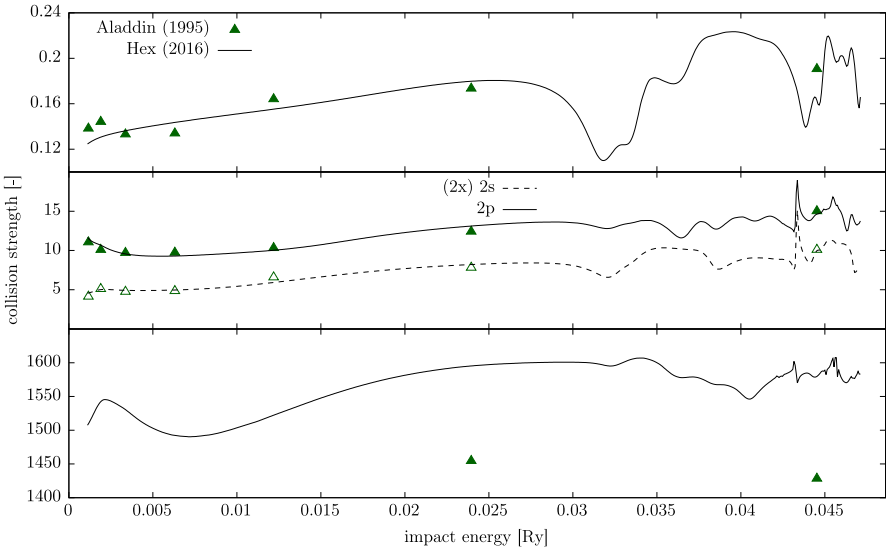

Graph 11. The collision strengths for the de-excitation from the state 3p to 1s (top panel), 2s and 2p (middle panel) states and the elastic scattering on 3p state (bottom panel).

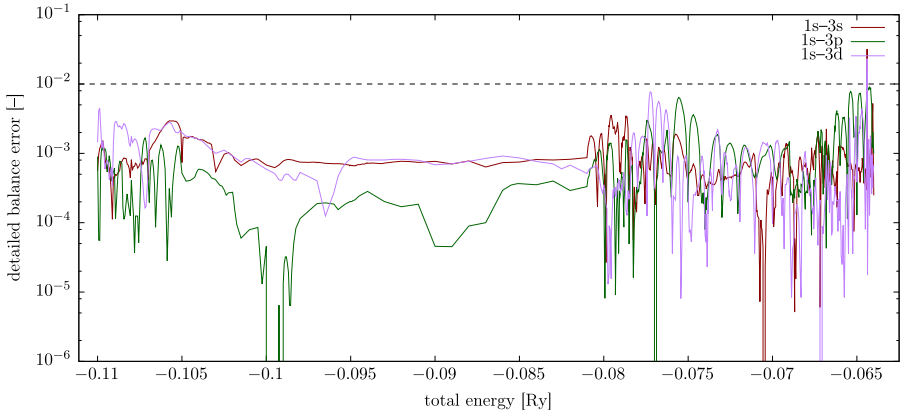

Graph 12. Detailed balance for 1s–3s, 1s–3p and 1s–3d transitions.

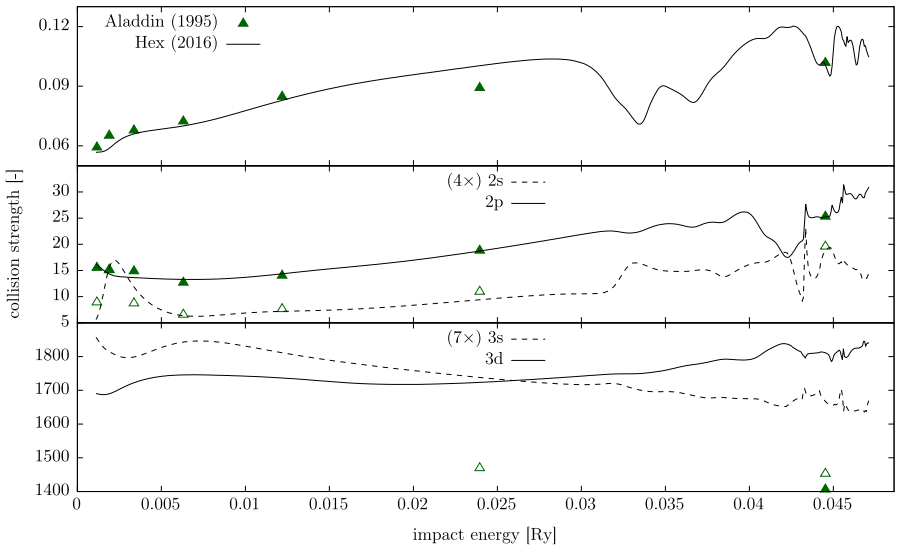

Graph 13. The collision strengths for the de-excitation from the state 3d to 1s (top panel), 2s and 2p (middle panel) states and the elastic scattering on the 3d state (bottom panel).

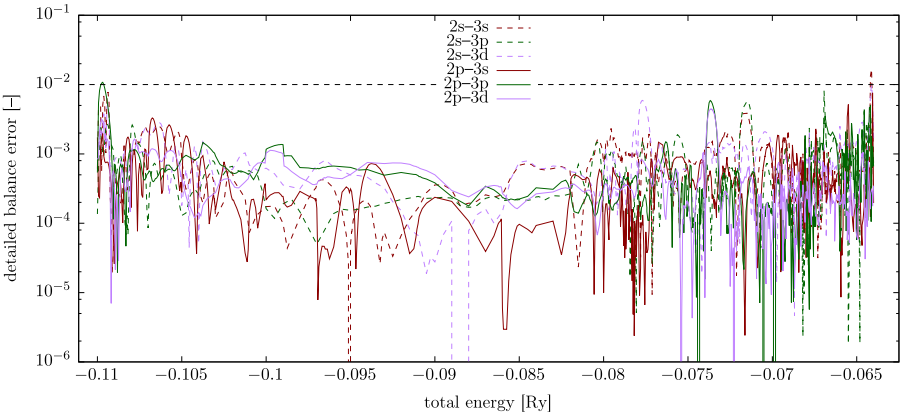

Graph 14. Detailed balance for 2ℓ–$3\ell'$ and $3\ell'$–2ℓ transitions.

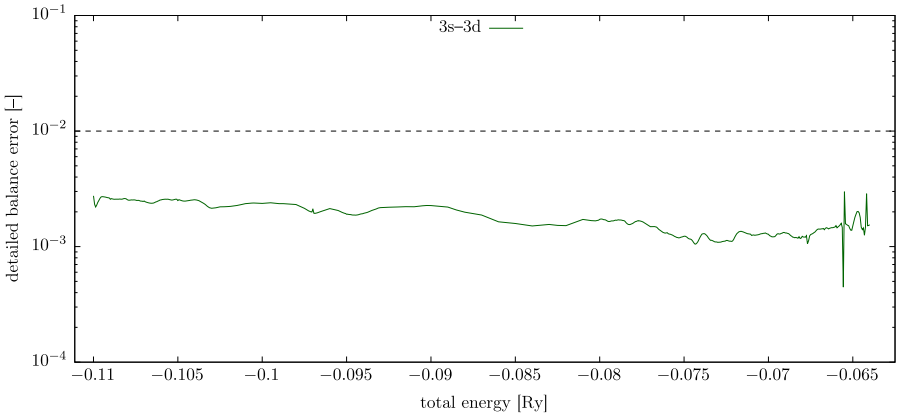

Graph 15. Detailed balance for the energetically degenerate transition 3s–3d.